

# Nanostructured Metal Carbides for Aprotic Li–O<sub>2</sub> Batteries: New Insights into Interfacial Reactions and Cathode Stability

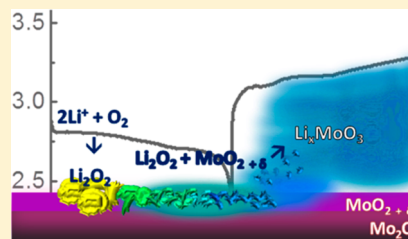
Dipan Kundu,<sup>†</sup> Robert Black,<sup>†</sup> Brian Adams,<sup>†</sup> Katharine Harrison,<sup>‡</sup> Kevin Zavadil,<sup>‡</sup> and Linda F. Nazar<sup>\*,†</sup>

<sup>†</sup>Department of Chemistry and the Waterloo Institute for Nanotechnology, University of Waterloo, Waterloo, Ontario, Canada N2L 3G1

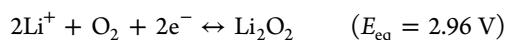
<sup>‡</sup>Sandia National Laboratory, Albuquerque, New Mexico 87185, United States

## S Supporting Information

**ABSTRACT:** The development of nonaqueous Li–oxygen batteries, which relies on the reversible reaction of Li + O<sub>2</sub> to give lithium peroxide (Li<sub>2</sub>O<sub>2</sub>), is challenged by several factors, not the least being the high charging voltage that results when carbon is typically employed as the cathode host. We report here on the remarkably low 3.2 V potential for Li<sub>2</sub>O<sub>2</sub> oxidation on a passivated nanostructured metallic carbide (Mo<sub>2</sub>C), carbon-free cathode host. Online mass spectrometry coupled with X-ray photoelectron spectroscopy unequivocally demonstrates that lithium peroxide is simultaneously oxidized together with the Li<sub>x</sub>MoO<sub>3</sub>-passivated conductive interface formed on the carbide, owing to their close redox potentials. The process rejuvenates the surface on each cycle upon electrochemical charge by releasing Li<sub>x</sub>MoO<sub>3</sub> into the electrolyte, explaining the low charging potential.



Rechargeable nonaqueous Li–O<sub>2</sub> batteries have garnered unprecedented interest in recent years due to their outstanding theoretical energy density ( $\sim 3000 \text{ W h kg}^{-1}$ )<sup>1,2</sup> that exceeds that of any other battery technologies. In its most common configuration, the Li–O<sub>2</sub> battery consists of a Li metal anode separated by a Li<sup>+</sup> conducting organic electrolyte from a porous carbon cathode. Upon discharge, Li<sup>+</sup> ions migrate through the electrolyte to the cathode and combine with O<sub>2</sub><sup>–</sup> to form LiO<sub>2</sub>, which then either electrochemically reduces or disproportionates to Li<sub>2</sub>O<sub>2</sub>. The charge reaction follows the reverse path, where the discharge product Li<sub>2</sub>O<sub>2</sub> is oxidized to generate O<sub>2</sub> at the cathode. This occurs at a thermodynamic potential of close to 3 V.<sup>3</sup>



The performance and rechargeability of Li–O<sub>2</sub> cells rely heavily on the cathode (positive electrode) material, where both oxygen reduction (ORR) and evolution (OER) take place.<sup>4–6</sup> Until very recently, carbon was the ubiquitous choice, but it has been shown to exhibit a large overpotential for Li<sub>2</sub>O<sub>2</sub> oxidation.<sup>7</sup> Polarization results from reactivity of the carbon surface with Li<sub>2</sub>O<sub>2</sub> and/or the reactive intermediate, LiO<sub>2</sub>,<sup>8,9</sup> to form a layer of insulating Li<sub>2</sub>CO<sub>3</sub> at the interface. The latter gives rise to cathode passivation, interfacial impedance, and high polarization upon cell charging, which in turn promotes electrolyte decomposition.<sup>10</sup> Extensive efforts have been made to find an alternative for carbon in the past few years. Materials with good ORR properties, high conductivity, and high chemical/electrochemical stability are emerging as feasible cathodes for next-generation Li–O<sub>2</sub> batteries. Among these, nanoporous gold, which shows high efficiency for Li<sub>2</sub>O<sub>2</sub> decomposition at a low overpotential, is very promising.<sup>11</sup>

However, it is clearly not suitable for practical applications. Cathodes based on oxides such as semiconducting Co<sub>3</sub>O<sub>4</sub>,<sup>12,13</sup> and V<sub>2</sub>O<sub>5</sub>,<sup>14</sup> and Al<sub>2</sub>O<sub>3</sub>-passivated carbon<sup>15</sup> have been employed to good effect, but these materials still present a significant impedance to electron transfer. Recently, Thiot et al. demonstrated nanocrystalline TiC as an efficient gas diffusion cathode.<sup>16</sup> It presents the qualities of metallic conductivity in common with gold. Upon electrochemical cycling, a passivating “TiO<sub>2</sub>-rich” surface layer is formed on TiC, rewarding long-term cyclability by helping to inhibit unwanted side reactions with the electrolyte or reduced oxygen species. However, the difficulty in reproducing these impressive results has baffled researchers in the field.<sup>17</sup> Our previous studies have shed some light on this by showing that OER upon charging Li<sub>2</sub>O<sub>2</sub> is directly related to the TiC cathode surface properties.<sup>18</sup> Oxidation of bulk (prefilled) peroxide is completely inhibited when approximately 2–3 nm of insulating TiO<sub>2</sub> covers the metallic TiC surface as a native oxide, whereas TiC that lacks this oxide layer, or in which the thin passivating film is <2 nm, allows charge transfer and effective OER. Precise control of the surface properties is thus of utmost importance. This principle found further validation in a Li–O<sub>2</sub> cell employing metallic Ti<sub>4</sub>O<sub>7</sub>, where a stable conductive TiO<sub>2–x</sub> interface is responsible for reversible Li<sub>2</sub>O<sub>2</sub> formation/decomposition.<sup>19</sup> A majority of the oxygen release occurs below 3.5 V versus Li<sup>+</sup>/Li, as demonstrated by online mass spectrometry (OEMS).

Received: April 7, 2015

Accepted: May 1, 2015

Published: May 1, 2015

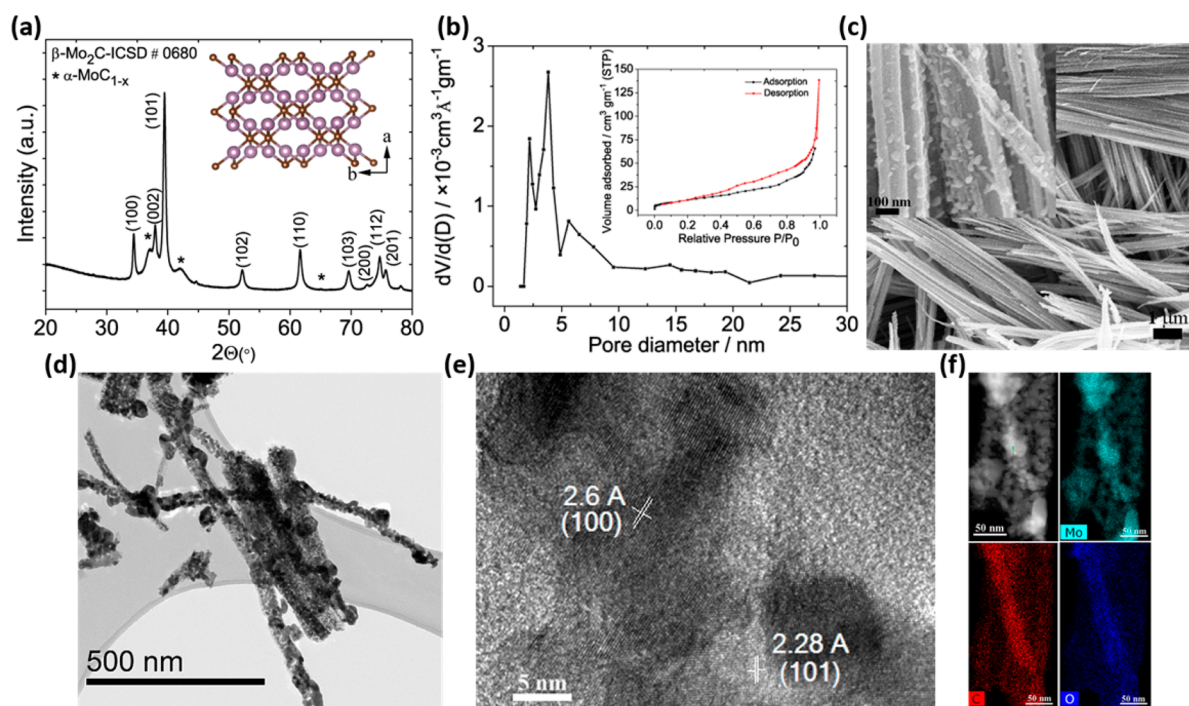


**Figure 1.** (a) Powder XRD pattern of the passivated  $\text{Mo}_2\text{C}$  nanofibers; the inset shows the arrangement of the Mo and C layers in the  $ab$  plane of the hexagonal crystal lattice. Mo and C are shown as purple and brown spheres, respectively. (b) Pore size distribution obtained by BJH analysis of the desorption branch of the  $\text{N}_2$ -sorption isotherm (shown as the inset image). (c) SEM images of the  $\text{Mo}_2\text{C}$  fibers. (d) Representative TEM image of the fibers. (e) High-resolution TEM image showing the lattice fringes in the nanocrystallites constituting the fibers. (f) High angle-annular dark field image (HAADF) of a region of a nanofiber with the electron energy loss spectroscopy (EELS) map of the constituent elements from the same region. The scale bars in (f) are all 50 nm.

Herein, we identify the unusual surface chemistry responsible for the behavior of nanoporous  $\text{Mo}_2\text{C}$ , which forms a native oxide ( $\text{MoO}_{2+\delta}$ ) and yields an anomalously low overpotential in a  $\text{Li}-\text{O}_2$  cell. Using OEMS and X-ray photoelectron spectroscopic (XPS) analysis, we show that the conductive oxide interface regenerates upon electrochemical cycling, retaining the electronically conductive surface essential for the effective charging of  $\text{Li}_2\text{O}_2$  but at the expense of consumption of the cathode.

Transition-metal carbides have attracted interest due to their outstanding thermal and electrical conductivities and excellent surface physiochemical properties arising from population of their d-orbital states near the Fermi level that resemble noble metals.<sup>20,21</sup>  $\beta\text{-Mo}_2\text{C}$  is one such material that is well-known for its catalytic activity in a wide variety of reactions, such as hydrodeoxygenation,<sup>22</sup> hydrogen evolution,<sup>20</sup> and  $\text{CO}_2$  conversion.<sup>23</sup> High surface area modifications prepared by thermal treatment of inorganic–organic hybrid precursors have shown promise in electrocatalysis.<sup>24</sup> Such a strategy allows controlled carbidization at the molecular level, leading to clean, nanostructured materials that are better than bulk products derived from thermal reduction of metal using hydrogen–hydrocarbon gas mixtures that result in contamination with carbon.

We developed a new hybrid precursor mediated approach to obtain elemental carbon-free nanostructured  $\text{Mo}_2\text{C}$ , which is crucial to investigate its carbon-independent ORR/OER properties in nonaqueous  $\text{Li}-\text{O}_2$  cells. Briefly, anilinium trimolybdate dihydrate  $[\text{Mo}_3\text{O}_{10}(\text{C}_6\text{H}_8\text{N})_2 \cdot 2\text{H}_2\text{O}]$  precursor was precipitated from an aniline and ammonium tetramolybdate solution in water by adjusting the pH to  $\sim 3\text{--}4$  (see the Experimental Methods section). X-ray diffraction (XRD) and scanning electron microscope (SEM) characterizations of this

precursor are provided in the Supporting Information (Figure S1a and b). The precursor was heat-treated at  $800^\circ\text{C}$  under flowing argon for 5 h to obtain  $\beta\text{-Mo}_2\text{C}$ . The treatment temperature was chosen based on thermogravimetric analysis (Figure S1c, Supporting Information) of the precursor under Ar, where two major weight loss segments ( $210$  and  $730^\circ\text{C}$ ) suggest formation of a stable phase beyond  $\sim 750^\circ\text{C}$ . The as-obtained  $\text{Mo}_2\text{C}$  was subjected to controlled passivation with  $1\%$   $\text{O}_2\text{--Ar}$  at  $25^\circ\text{C}$  before exposing it to an ambient atmosphere because nanometric carbides are highly pyrophoric.<sup>25</sup> Partial oxidation forms a thin film of metallic  $\text{MoO}_{2+\delta}$  on the outer surface (see below), leaving the bulk of the material intact.

Formation of  $\text{Mo}_2\text{C}$  was confirmed by XRD (Figure 1a).  $\text{Mo}_2\text{C}$  crystallizes in the  $\beta$  form with hexagonal ABAB packing of the metal atom layers, as shown in the inset of Figure 1a. XRD also reveals the presence of a small amount of  $\alpha\text{-MoC}_{1-x}$  formed as a result of incomplete carbidization. A Brunauer–Emmett–Teller (BET)-specific surface area of  $50\text{ m}^2\text{ g}^{-1}$  was obtained from the nitrogen sorption isotherm (Figure 1b). It exhibits a type-IV hysteresis, indicating the presence of meso/macroscopic porosity. Barrett–Joyner–Halenda (BJH) analysis of the desorption branch of the isotherm revealed a pore size distribution peaking at  $\sim 3\text{--}4$  nm. Further insight into the morphology was obtained by SEM and transmission electron microscopic (TEM) studies. SEM shows that the material adopts a nanofiber morphology with bundled, stacked fibers of average diameter  $\sim 100$  nm (Figure 1c and inset). The fibers are comprised of loosely interconnected crystallites ( $\sim 10$  nm diameter) that lead to the porous architecture (TEM, Figure 1d). The porosity is a direct outcome of the thermochemical synthesis, where molecular association between the inorganic and organic components facilitates a near-homogeneous

carbide process, leading to interconnected nanocrystallites. TEM analysis did not show the presence of any carbon particles on the  $\text{Mo}_2\text{C}$  nanoparticles/fibers, and high-resolution TEM (HRTEM) resolved the (100) and (101)  $\text{Mo}_2\text{C}$  lattice fringes (Figure 1e). The lack of bulk carbon was also demonstrated by elemental mapping recorded of a single nanofiber showing a uniform distribution of Mo, C, and O (Figure 1f). The oxygen arises from the passivating molybdenum oxide layer on the surface, as confirmed by X-ray photoelectron spectroscopy (XPS, Figure S2 and Table S1, Supporting Information). The surface of  $\text{Mo}_2\text{C}$  is always contaminated with Mo oxide species in fact,<sup>20,21</sup> which are formed during controlled passivation of the as-synthesized material in our case. Accordingly, the Mo 3d XPS spectra of the fibers were fit with a classic contribution of species ranging from  $\text{Mo}^0$  to  $\text{Mo}^{6+}$ , as previously described for  $\text{Mo}_2\text{C}$ .<sup>20,23</sup> The surface Mo species ( $\text{Mo}^{2+}$ – $\text{Mo}^{6+}$ ) exhibit an average oxidation state of  $\text{Mo}^{4.1+}$  (i.e.,  $\text{MoO}_{2+\delta}$ ),<sup>26</sup> as summarized in the quantitative analysis shown in Figure 2. Owing to the well-

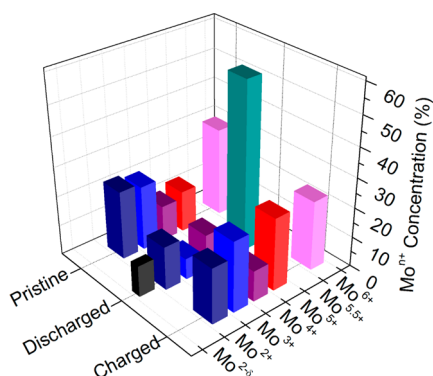


**Figure 2.** Quantitative representation of the  $\text{Mo}_2\text{C}$  electrode surface obtained from in-depth XPS studies of the pristine, discharged, and charged cathode after galvanostatic discharge/charge in a  $\text{Li}-\text{O}_2$  cell with 0.5 M LiTFSI-TEGDME as the electrolyte. The assigned oxidation states of the Mo species are approximated in accord with well-known values from the literature reported for  $\text{Mo}_2\text{C}$ <sup>21</sup> and Mo oxides as summarized in the XPS Handbook.<sup>26</sup> See the Supporting Information for additional details on XPS spectra and fitting.

known metallic properties of the underlying  $\text{Mo}_2\text{C}$  and that of the Mo suboxides, the active surface is expected to be highly electrically conductive.<sup>27</sup> Coordinatively unsaturated Mo states on the  $\text{Mo}_2\text{C}$  surface are thought to be responsible for its high catalytic activity for dehydrogenation and electrochemical hydrogen evolution.<sup>24</sup> These metal centers are also expected to have strong affinity for oxygen, thus favoring a surface-mediated ORR process (see below). The one-dimensional  $\beta$ - $\text{Mo}_2\text{C}$  fibers additionally possess key attributes such as enriched mesoporosity, and a large surface area, which—along with offering abundant surface specific sites—facilitate electrolyte percolation and good charge-transfer kinetics.

The ORR and OER performance of the  $\text{Mo}_2\text{C}$  was investigated in nonaqueous  $\text{Li}-\text{O}_2$  cells (see the Supporting Information for details). Two electrolytes were explored, 0.5 M lithium bis(trifluoromethanesulfonyl) imide (LiTFSI) in tetraethylene glycol dimethyl ether (TEGDME) and 0.5 M  $\text{LiClO}_4$  in dimethylsulfoxide (DMSO). The latter was investigated because of the better solubility of lithium superoxide in DMSO,<sup>28</sup> in order to explore its effect on the discharge capacity and OER overpotential. Compatibility of the  $\text{Mo}_2\text{C}$  cathode

with these electrolytes was established by discharging/charging the cells at constant current under Ar. The TEGDME-based electrolyte demonstrates good stability below 4 V, with electrolyte oxidation commencing at  $\sim 4.65$  V (Figure S3a, Supporting Information). DMSO, however, exhibits pronounced parasitic processes upon charging above  $\sim 3.6$  V, which start as low as 3.25 V (Figure S3b, Supporting Information). Therefore, TEGDME was used for the XPS investigation of the cycled cathode and for the quantification of the oxygen reaction. Cells were discharged to 2.4 V at a constant current density of  $100 \mu\text{A cm}^{-2}$ . The total oxygen consumption was monitored with OEMS while the cell was electrochemically discharged to a capacity of  $0.5 \text{ mA h/cm}^2$ . This provides a direct correlation between the oxygen consumption and the coulometric process. Discharge of the cell showed a linear decrease in the total amount of consumed oxygen throughout the entirety of discharge. The ratio of moles of electron passed to the moles of  $\text{O}_2$  consumed ( $e^-/\text{O}_2$ ) is 2.05, close to the value of 2.0 expected for an ideal ( $2\text{Li}^+ + \text{O}_2 \rightarrow \text{Li}_2\text{O}_2$ ) reaction (Figure 3a). Our value is comparable to the value reported by McCloskey et al. for glyme-based electrolytes<sup>29</sup> and suggests predominant formation of  $\text{Li}_2\text{O}_2$  along with a minor degree of side reactions. Quantification of the peroxide content by iodometric titration was not possible because, unlike carbon-based cathodes, the native transition-metal oxide formed on the surface of the carbides participates in the redox reaction with the liberated iodine that is the basis of the titration. However, formation of  $\text{Li}_2\text{O}_2$  upon cell discharge was confirmed by ex situ XPS. The Li 1s peak at 54.9 eV corresponding to  $\text{Li}_2\text{O}_2$ <sup>30</sup> characterizes the discharged cathode (Figure 3b) and disappears upon charging the cell to 3.6 V. Some  $\text{Li}_2\text{CO}_3$  (Li 1s at 55.5 eV) remains on the surface after charge, which we ascribe to electrolyte degradation.

The formation of  $\text{Li}_2\text{O}_2$  is also signaled by the cycling profile for the TEGDME-based cell that shows a typical ORR plateau at 2.6 V vs  $\text{Li}^+/\text{Li}$  (Figure 3c). A moderate discharge capacity is delivered at  $100 \mu\text{A cm}^{-2}$ , and operating the cell at lower or higher current densities ( $25\text{--}200 \mu\text{A cm}^{-2}$ ) has little influence. Among many factors that may affect the capacity and rate capability, the mechanism of  $\text{O}_2$  reduction and the resultant product morphology play important roles.<sup>28,31,32</sup> A dominant surface pathway leads to obstruction of the active ORR surface sites due to the growth of insulating surface films of  $\text{Li}_2\text{O}_2$ . Thick films ultimately exhibit limited charge transfer. Conversely, in a solution-mediated process that results in crystallization of  $\text{Li}_2\text{O}_2$  from solution as plates or “toroids”, the active surface sites remain accessible for longer duration, resulting in higher capacities. The morphology of the  $\text{Li}_2\text{O}_2$ , probed by SEM, showed that in both TEGDME and DMSO, a film-like product is observed (Figure S4, Supporting Information). The lack of platelets or crystalline aggregates proves that a surface-mediated discharge process predominates. The high ORR activity/strong  $\text{O}_2$  coordination of the  $\text{Mo}_2\text{C}$  surface may contribute to the surface reaction. Insulating  $\text{Li}_2\text{O}_2$  film formation leads to a buildup of overpotential with increasing discharge depth for TEGDME and hence low capacity. Accordingly, DMSO as an electrolyte, known to solvate lithium superoxide much more efficiently than TEGDME, gave rise to a much higher discharge capacity of  $\sim 1.8 \text{ mA h}$  (Figure 3d). The average discharge voltage of 2.7 V is indicative of less polarization and/or more efficient charge transfer at the interface. The capacity of  $1.8 \text{ mA h}$  ( $600\text{--}700 \text{ mA h g}^{-1}$  of carbide) is comparable to that observed for TiC



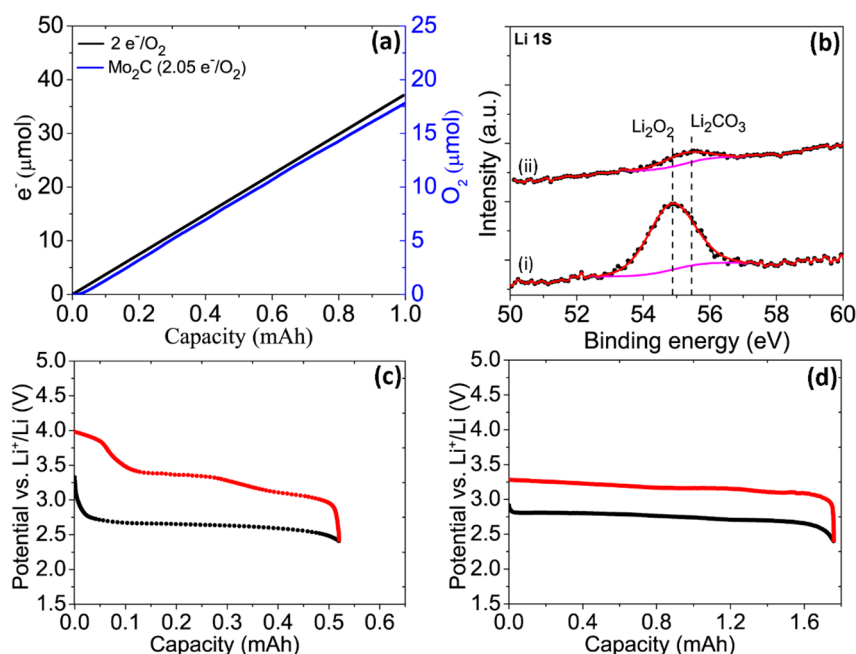
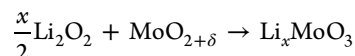


**Figure 3.** (a) Quantification of the oxygen consumption with respect to the charge passed during the discharge reaction in a Li–O<sub>2</sub> cell employing 0.5 M LiTFSI-TEGDME as the electrolyte. (b) Li 1s region of the XPS spectra of the Mo<sub>2</sub>C cathode after galvanostatic discharge (i) and charge (ii) using a LiTFSI-TEGDME-based electrolyte. Galvanostatic discharge–charge profiles of the Mo<sub>2</sub>C fiber-based gas diffusion cathode in Li–O<sub>2</sub> cells at a current density of 100  $\mu\text{A cm}^{-2}$  with a 1.0 cm<sup>2</sup> cathode using (c) 0.5 M LiTFSI-TEGDME and (d) 0.5 M LiClO<sub>4</sub>-DMSO electrolytes.

cathode materials utilized in Li–O<sub>2</sub> cells under comparable conditions, after accounting for the difference in mass of the cathode host.<sup>16</sup> Similar to that study, where a thin film of TiO<sub>2</sub> was formed on the TiC surface upon discharge, we also observe a change in the surface-passivating oxide in the Mo 3d XPS spectrum. The increase in the average oxidation state to  $\sim\text{Mo}^{5.5+}$  indicates an interfacial reaction of the type



(where  $x$  is  $\sim 0.5$  based on XPS analysis; Figure S2 and Table S1, Supporting Information)

This reaction is thermodynamically driven by a negative  $\Delta G_p$  as is the reaction of Li<sub>2</sub>O<sub>2</sub> with carbon, namely,  $\text{Li}_2\text{O}_2 + \frac{1}{2}\text{O}_2 + \text{C} = \text{Li}_2\text{CO}_3$ , reported by McCloskey et al.<sup>9</sup> The difference is that the insulating, insoluble nature of Li<sub>2</sub>CO<sub>3</sub> curtails charge transfer and leads to high impedance upon charge. In contrast, the electronically conductive properties of Li<sub>x</sub>MoO<sub>3</sub> and its ability to readily form a colloidal dispersion at low values of  $x$  lead to the opposite, namely, “self-cleaning” of the metallic carbide surface, as described below.

The most notable feature of the discharge/charge profile of Mo<sub>2</sub>C in TEGDME (Figure 3c) is the remarkably low charge overpotential; approximately  $\sim 90\%$  of charge is apparently complete by 3.5 V. The voltage (3.3 V) is even lower for DMSO (Figure 3d). Removal of the Li<sub>2</sub>O<sub>2</sub> film upon subsequent charge is evident from the Li 1s XPS spectra (see above) and also from the SEM images of the respective cathodes (Figure S4, Supporting Information). The Mo 3d core-level XPS spectra of the charged cathode shows that the features and average oxidation state of the pristine material ( $\sim\text{Mo}^{4+}$ , i.e., MoO<sub>2 $\pm\delta$</sub> ) are largely recovered, indicating loss of the oxidized Mo<sup>5.5+</sup> component (Figures 2 and S2, Supporting Information). Regeneration of the cathode interface upon charge suggests that the interfacial electrical conductivity should be regained, along with re-exposure of the catalytically active

unsaturated Mo states. The retention of the catalytically active surface is evident from sustainable ORR and a low-voltage OER process during extended cycling of the Li–O<sub>2</sub> cell employing both TEGDME- and DMSO-based electrolytes (Figure S5, Supporting Information).

To fully understand the nature of the charge process, we monitored gas evolution from the cell during oxidation using OEMS cells with a larger surface area.<sup>9,29</sup> The cells were first discharged to a capacity of 1 mA h and then charged to measure the evolution of gaseous oxygen ( $m/z = 32$ ) and carbon dioxide ( $m/z = 44$ ). The results are shown in Figure 4 and are representative of multiple cells that were examined. At the onset of charge, O<sub>2</sub> was evolved but not in the quantities expected. Moreover, initial oxygen release was followed by its diminution as charge progresses. The slight increase in O<sub>2</sub> evolution at around 3.4 V (0.85 mA h) may be due to the exposure of some residual Li<sub>2</sub>O<sub>2</sub> that was initially occluded as

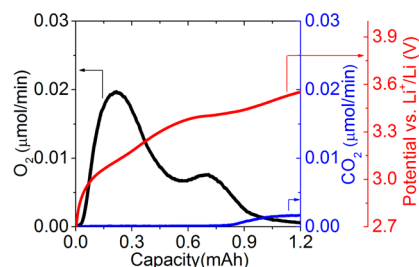


**Figure 4.** Online electrochemical mass spectrometry (OEMS) for the cell employing a 2.0 cm<sup>2</sup> Mo<sub>2</sub>C cathode in 0.5 M LiTFSI-TEGDME during electrochemical charge of a cell pre-discharged to a capacity of 1 mA h (i.e., 0.5 mA h/cm<sup>2</sup>). The red, black, and blue curves depict voltage variation, O<sub>2</sub> evolution, and CO<sub>2</sub> evolution, respectively, during galvanostatic charge. A 2e<sup>-</sup>/O<sub>2</sub> process would correspond to an OER rate of 0.062  $\mu\text{mol/min}$ . Cell charging was performed at 100  $\mu\text{A cm}^{-2}$  preceded by a 5 h rest period at OCV after discharge.

other contaminants were stripped off (see below). A very small amount of  $\text{CO}_2$  evolution was also observed at around 3.6 V, resulting from the oxidation of electrolyte decomposition products such as lithium acetate and formate.<sup>33</sup> By combining OER with the charge current, we calculated a ratio of  $(e^-/\text{O}_2)_{\text{chg}}$ , which is a measure of the Coulombic efficiency. The value should be 2.0 if the only process upon charge is the oxidation of lithium peroxide. Most studies show  $(e^-/\text{O}_2)_{\text{chg}} \approx 2.4\text{--}2.6$ , which implies that some parasitic electrochemistry occurs during the charging process.<sup>49</sup> The TEGDME/ $\text{Mo}_2\text{C}$  cell exhibits an extremely high  $(e^-/\text{O}_2)_{\text{chg}}$  ratio of 11.6, however, indicative of an additional and major electrochemical contribution. Similar results were observed in a DMSO/ $\text{Mo}_2\text{C}$  cell, except that lower OER was detected upon charge compared to that of the TEGDME/ $\text{Mo}_2\text{C}$  cell (Figure S6, Supporting Information), hence resulting in a higher ( $>15$ )  $(e^-/\text{O}_2)_{\text{chg}}$  ratio.

This is explained by accounting for the fate of the  $\text{Li}_x\text{MoO}_3$  formed upon discharge. On the charge cycle, this material will be oxidized to form  $\text{Li}_y\text{MoO}_3$  (where  $y < x$ ) because its redox potential coincidentally falls in the same voltage region as that of the  $\text{Li}_2\text{O}_2/\text{O}_2$  couple.<sup>34</sup> It is well established that at low values of lithium intercalation,  $\text{Li}_y\text{MoO}_3$  readily disperses into polar media to form deep blue colloidal solutions containing exfoliated nanosheets of  $\text{MoO}_3^{y-}$ .<sup>35</sup> This process partially “cleans” the surface. In accord, post-mortem analysis of cells revealed a deep blue product in the separator/electrolyte (Figure S7a, Supporting Information), with the color intensifying upon each cycle of the cell. Energy dispersive X-ray spectroscopy (EDX) analysis of the product clogged in the glass fiber separator revealed a 1:3 atomic ratio of Mo/O, as expected (Figure S8, Supporting Information; Li is not visible by EDX). Chemical lithiation of  $\text{MoO}_3$  also confirmed the characteristic deep blue color of lithiated  $\text{MoO}_3$  and its facile dispersibility in TEGDME and particularly DMSO (Figure S7b, Supporting Information). Thus, the competitive oxidation of  $\text{Li}_2\text{O}_2$  and  $\text{Li}_x\text{MoO}_3$  leads to the removal of much of the passivating surface molybdenum oxide layer of the carbide, but the surface becomes repassivated on each cycle upon reaction with  $\text{O}_2$ ,  $\text{Li}_2\text{O}_2$ , or superoxide. Repeated cycling of surface  $\text{MoO}_x$  lithiation/stripping accumulates colloidal  $\text{MoO}_3^{y-}$  in the separator/electrolyte (Figures S7b and 8, Supporting Information), resulting in a viscous electrolyte and ultimately shutting down cell performance.

In conclusion, we demonstrate that high surface area nanoporous  $\text{Mo}_2\text{C}$  nanofibers, generated by a thermochemical approach, are very active for aprotic ORR. Controlled surface passivation results in their coverage with a nanometric layer of conductive  $\text{MoO}_{2+\delta}$ , driving a dominant surface-mediated ORR reaction in the  $\text{Li}-\text{O}_2$  cell that results in a film-like  $\text{Li}_2\text{O}_2$  product. This passivates the surface and results in lower capacity.  $\text{TiC}$ , on the other hand, forms a different, more coordinatively saturated oxide<sup>16,18</sup> (owing to the narrower available range of Ti valence states) and thus operates by a solution-mediated ORR mechanism<sup>32</sup> at comparable current densities. We further show that the complex surface chemistry of ORR/OER materials for  $\text{Li}-\text{O}_2$  batteries can lead to unanticipated results. First and foremost, the thermodynamic instability of low-valent metallic carbides in the presence of oxidizing species always leads to oxide passivation layers on their surfaces. These layers can be benign and beneficial as for  $\text{TiC}$  or  $\text{Ti}_4\text{O}_7$  when the oxide ( $\text{TiO}_{2-\delta}$ ) is conductive and stable or lead to parasitic oxidation upon charge, as in the case of

$\text{Mo}_2\text{C}$ . Competitive oxidation of the passivating  $\text{MoO}_{2+\delta}$  surface layer and its subsequent dissolution regenerates the active cathode interface upon electrochemical charge, exposing the conductive surface that also promotes  $\text{Li}_2\text{O}_2$  oxidation at low overpotential. However, that same competitive oxidation also leads to very poor Coulombic efficiency and to the accumulation of undesired products in the electrolyte upon cycling. Second, our study shows the critical importance of using OEMS to quantify OER and “real” rechargeability of the cell in the face of potentially misleading electrochemical reactivity (*caveat lector*). Finally, our results provide a predictive analysis for development of  $\text{Li}-\text{O}_2$  host materials, strongly suggesting that carbides such as  $\text{W}_2\text{C}$  and  $\text{VC}$  will also not be suitable owing to similar formation of surface oxides (ie,  $\text{WO}_x$ ,  $\text{V}_2\text{O}_{5-x}$ ) that are expected to have redox activity in the same voltage range as  $\text{Li}_2\text{O}_2$ . On the other hand, an understanding of the surface reactivity provides guidelines for the search of new promising carbides and other materials that may possess excellent cathode host properties.

## ■ EXPERIMENTAL METHODS

**Synthesis of  $\text{Mo}_2\text{C}$  Fibers.** The  $\text{Mo}_2\text{C}$  nanofibers were synthesized by thermal decomposition of the as-synthesized anilinium trimolybdate fibers at 800 °C under an argon flow (see the Supporting Information for details). The  $\text{Mo}_2\text{C}$  was passivated under a 1%  $\text{O}_2$ /balance argon flow for 4 h before exposing it to ambient atmosphere.

**Characterization.** Powder XRD was carried out using a Bruker D8 Advance diffractometer in Bragg–Brentano geometry with  $\text{CuK}\alpha$  ( $\lambda = 1.5405$  Å) radiation. SEM was performed on a LEO 1530 field emission SEM (FESEM) equipped with an EDX attachment. TEM was conducted on an FEI Titan S/TEM platform operated at 200 kV, where the elemental mapping of Mo, C, and O was carried out using the EELS spectra imaging function. Thermogravimetric analysis (TG-DTA) was performed using a TA Instruments SDT Q600 in air at a heating rate of 5 °C  $\text{min}^{-1}$ . Nitrogen adsorption–desorption analyses were performed at 77 K on a Quantachrome AUTOSORB-1, first outgassing the sample for 12 h at 200 °C under vacuum. XPS analysis was performed on a Thermo ESCALAB 250 instrument configured with monochromatic  $\text{Al K}\alpha$  (1486.6 eV). The air-sensitive samples were transported to the spectrometer in an Ar atmosphere and transferred into the chamber with less than a 5 s exposure to ambient. All spectra were fitted with Gaussian–Lorentzian functions and a Shirley-type background using CasaXPS software. The binding energy values were all calibrated using the adventitious C 1s peak at 284.8 eV.

**Electrochemical Studies.** Electrochemical properties were assessed using hermetically sealed Swagelok-type cells, assembled using 1.0  $\text{cm}^2$  cathodes with Li metal foil as the anode and a glass fiber membrane as the separator. Solutions of 0.5 M LiTFSI-TEGDME or 0.5 M  $\text{LiClO}_4$ -DMSO were used as the electrolyte. Galvanostatic cycling was performed using a BT2000 battery cycler (Arbin Instruments). The current densities reported in this work are based on the geometric electrode area.

**Online Electrochemical Mass Spectrometry (OEMS).** The residual gas analysis was performed using a modified version of an OEMS apparatus reported by Tsiouvaras et al.,<sup>36</sup> employing 2.0  $\text{cm}^2$  stainless steel mesh electrodes. The  $e^-/\text{O}_2$  values were determined from the total accumulated amount of  $\text{O}_2$  by comparison to the coulometric capacity.

## ■ ASSOCIATED CONTENT

## ■ Supporting Information

Detailed experimental methods, XRD, SEM, and thermal analysis of the precursor, Mo 3d core-level XPS analysis of the pristine and cycled cathode, galvanostatic discharge–charge profile of the Mo<sub>2</sub>C cathode under an Ar atmosphere, extended galvanostatic cycling data, post-mortem analysis of the cell component, and results on the chemical lithiation of MoO<sub>3</sub>. The Supporting Information is available free of charge on the ACS Publications website at DOI: 10.1021/acs.jpclett.5b00721.

## ■ AUTHOR INFORMATION

## Corresponding Author

\*E-mail: lfnazar@uwaterloo.ca.

## Notes

The authors declare no competing financial interest.

## ■ ACKNOWLEDGMENTS

We gratefully acknowledge NRCan for funding through their EcoEII program. We thank NSERC for partial financial support through their Discovery Grant and Chair programs, and B.A., K.H., and K.Z. acknowledge partial support of the research as part of the Joint Center for Energy Storage Research, an Energy Innovation Hub funded by the U.S. Department of Energy, Office of Science, Basic Energy Sciences. The authors gratefully acknowledge Paul G. Kotula (Sandia National Laboratories) for TEM analysis.

## ■ REFERENCES

- (1) Bruce, P. G.; Freunberger, S. A.; Hardwick, L. J.; Tarascon, J.-M. Li–O<sub>2</sub> and Li–S Batteries with High Energy Storage. *Nat. Mater.* **2012**, *11*, 19–29.
- (2) Black, R.; Adams, B.; Nazar, L. F. Non-Aqueous and Hybrid Li–O<sub>2</sub> Batteries. *Adv. Energy Mater.* **2012**, *2*, 801–815.
- (3) Cui, Z. H.; Guo, X. X.; Li, H. Equilibrium Voltage and Overpotential Variation of Nonaqueous Li–O<sub>2</sub> Batteries Using the Galvanostatic Intermittent Titration Technique. *Energy Environ. Sci.* **2015**, *8*, 182–197.
- (4) Lu, Y.-C.; Shao-Horn, Y. Probing the Reaction Kinetics of the Charge Reactions of Nonaqueous Li–O<sub>2</sub> Batteries. *J. Phys. Chem. Lett.* **2013**, *4*, 93–99.
- (5) Black, R.; Lee, J.-H.; Adams, B.; Mims, C. A.; Nazar, L. F. The Role of Catalysts and Peroxide Oxidation in Lithium–Oxygen Batteries. *Angew. Chem.* **2013**, *52*, 392–396.
- (6) Lu, Y.-C.; Gasteiger, H. A.; Parent, M. C.; Chiloyan, V.; Shao-Horn, Y. The Influence of Catalysts on Discharge and Charge Voltages of Rechargeable Li–Oxygen Batteries. *Electrochem. Solid-State Lett.* **2010**, *13*, A69–A72.
- (7) Li, F.; Zhang, T.; Zhou, H. Challenges of Non-Aqueous Li–O<sub>2</sub> Batteries: Electrolytes, Catalysts, and Anodes. *Energy Environ. Sci.* **2013**, *6*, 1125–1141.
- (8) Itkis, D. M.; Semenenko, D. A.; Kataev, E. Y.; Belova, A. I.; Neudachina, V. S.; Sirotna, A. P.; Havecker, M.; Teschner, D.; Knop-Gericke, A.; Dudin, P.; et al. Reactivity of Carbon in Lithium–Oxygen Battery Positive Electrodes. *Nano Lett.* **2013**, *13*, 4697–4701.
- (9) McCloskey, B. D.; Speidel, A.; Scheffler, R.; Miller, D. C.; Viswanathan, V.; Hummelshøj, J. S.; Nørskov, J. K.; Luntz, A. C. Twin Problems of Interfacial Carbonate Formation in Nonaqueous Li–O<sub>2</sub> Batteries. *J. Phys. Chem. Lett.* **2012**, *3*, 997–1001.
- (10) Thotiyl, M. M. O.; Freunberger, S. A.; Peng, Z.; Bruce, P. G. The Carbon Electrode in Nonaqueous Li–O<sub>2</sub> Cells. *J. Am. Chem. Soc.* **2012**, *135*, 494–500.
- (11) Peng, Z.; Freunberger, S. A.; Chen, Y.; Bruce, P. G. A Reversible and Higher-Rate Li–O<sub>2</sub> Battery. *Science* **2012**, *337*, 563–566.
- (12) Cui, Y.; Wen, Z.; Liu, Y. A Free-Standing-Type Design for Cathodes of Rechargeable Li–O<sub>2</sub> Batteries. *Energy Environ. Sci.* **2011**, *4*, 4727–4734.
- (13) Riaz, A.; Jung, K.-N.; Chang, W.; Lee, S.-B.; Lim, T.-H.; Park, S.-J.; Song, R.-H.; Yoon, S.; Shin, K.-H.; Lee, J.-W. Carbon-Free Cobalt Oxide Cathodes with Tunable Nanoarchitectures for Rechargeable Lithium–Oxygen Batteries. *Chem. Commun.* **2013**, *49*, 5984–5986.
- (14) Lu, Y.-C.; Crumlin, E. J.; Veith, G. M.; Harding, J. R.; Mutoro, E.; Baggetto, L.; Dudney, N. J.; Liu, Z.; Shao-Horn, Y. In Situ Ambient Pressure X-ray Photoelectron Spectroscopy Studies of Lithium–Oxygen Redox Reactions. *Sci. Rep.* **2012**, *2*, 715.
- (15) Lu, J.; Lei, Y.; Lau, K. C.; Luo, X.; Du, P.; Wen, J.; Assary, R. S.; Das, U.; Miller, D. J.; Elam, J. W.; et al. Nanostructured Cathode Architecture for Low Charge Overpotential in Lithium–Oxygen Batteries. *Nat. Commun.* **2013**, *4*, 2383.
- (16) Thotiyl, M. M. O.; Freunberger, S. A.; Peng, Z.; Chen, Y.; Liu, Z.; Bruce, P. G. A Stable Cathode for the Aprotic Li–O<sub>2</sub> Battery. *Nat. Mater.* **2013**, *12*, 1050–1056.
- (17) Luntz, A. C.; McCloskey, B. D. Nonaqueous Li–Air Batteries: A Status Report. *Chem. Rev.* **2014**, *114*, 11721–11750.
- (18) Adams, B. D.; Black, R.; Radtke, C.; Williams, Z.; Mehdi, B. L.; Browning, N. D.; Nazar, L. F. The Importance of Nanometric Passivating Films on Cathodes for Li–Air Batteries. *ACS Nano* **2014**, *8*, 12483–12493.
- (19) Kundu, D.; Black, R.; Berg, E. J.; Nazar, L. F. A Highly Active Nanostructured Metallic Oxide Cathode for Aprotic Li–O<sub>2</sub> Batteries. *Energy Environ. Sci.* **2015**, *8*, 1292–1298.
- (20) Wan, C.; Regmi, Y. N.; Leonard, B. M. Multiple Phases of Molybdenum Carbide as Electrocatalysts for the Hydrogen Evolution Reaction. *Angew. Chem., Int. Ed.* **2014**, *53*, 6407–6410.
- (21) Li, Z.; Chen, C.; Zhan, E.; Ta, N.; Li, Y.; Shen, W. Crystal-Phase Control of Molybdenum Carbide Nanobelts for Dehydrogenation of Benzyl Alcohol. *Chem. Commun.* **2014**, *50*, 4469–4471.
- (22) Ren, H.; Yu, W.; Saliccioli, M.; Chen, Y.; Huang, Y.; Xiong, K.; Vlachos, D. G.; Chen, J. G. Selective Hydrodeoxygenation of Biomass-Derived Oxygenates to Unsaturated Hydrocarbons Using Molybdenum Carbide Catalysts. *ChemSusChem* **2013**, *6*, 798–801.
- (23) Porosoff, M. D.; Yang, X.; Boscoboinik, J. A.; Chen, J. G. Molybdenum Carbide as Alternative Catalysts to Precious Metals for Highly Selective Reduction of CO<sub>2</sub> to CO. *Angew. Chem., Int. Ed.* **2014**, *53*, 6705–6709.
- (24) Liao, L.; Wang, S.; Xiao, J.; Bian, X.; Zhang, Y.; Scanlon, M. D.; Hu, X.; Tang, Y.; Liu, B.; Girault, H. H. A Nanoporous Molybdenum Carbide Nanowire as an Electrocatalyst for Hydrogen Evolution Reaction. *Energy Environ. Sci.* **2014**, *7*, 387–392.
- (25) Kotarba, A.; Adamski, G.; Sojka, Z.; Djega-Mariadassou, G.; Pettersson, J. B. C. In Situ Monitoring of Bare and K-Doped Mo<sub>2</sub>C Catalysts Surface Depassivation Based on Emission of Electrons and K<sup>+</sup> Ions. *Appl. Surf. Sci.* **2006**, *252*, 4129–4137.
- (26) Moulder, J. F.; Stickle, W. F.; Sobol, P. E.; Bomben, K. D. *Handbook of X-ray Photoelectron Spectroscopy*; Perkin-Elmer Corporation: Eden Prairie, MN, 1992.
- (27) Li, Z.; Schram, T.; Witters, T.; Cho, H. J.; O'Sullivan, B.; Yamada, N.; Takaaki, T.; Hooker, J.; Gendt, S. D.; Meyera, K. D. Investigation on Molybdenum and Its Conductive Oxides as p-Type Metal Gate Candidates. *J. Electrochem. Soc.* **2008**, *7*, H481–H484.
- (28) Johnson, L.; Li, C.; Liu, Z.; Chen, Y.; Freunberger, S. A.; Tarascon, J.-M.; Ashok, P. C.; Praveen, B. B.; Dholakia, K.; Bruce, P. G. The Role of LiO<sub>2</sub> Solubility in O<sub>2</sub> Reduction in Aprotic Solvents and Its Consequences for Li–O<sub>2</sub> Batteries. *Nat. Chem.* **2014**, *6*, 1091–1099.
- (29) McCloskey, B. D.; Bethune, D. S.; Shelby, R. M.; Girishkumar, G.; Luntz, A. C. Solvents' Critical Role in Nonaqueous Lithium–Oxygen Battery Electrochemistry. *J. Phys. Chem. Lett.* **2011**, *2*, 1161–1166.
- (30) Younesi, R.; Urbonaite, S.; Edström, K.; Hahlin, M. The Cathode Surface Composition of a Cycled Li–O<sub>2</sub> Battery: A Photoelectron Spectroscopy Study. *J. Phys. Chem. C* **2012**, *116*, 20673–20680.

- (31) Laoire, C. O.; Mukerjee, S.; Abraham, K. M.; Plichta, E. J.; Hendrickson, M. A. Elucidating the Mechanism of Oxygen Reduction for Lithium–Air Battery Applications. *J. Phys. Chem. C* **2009**, *113*, 20127–20134.
- (32) Adams, B. D.; Radtke, C.; Black, R.; Trudeau, M. L.; Zaghib, K.; Nazar, L. F. Current Density Dependence of Peroxide Formation in the Li–O<sub>2</sub> Battery and Its Effect on Charge. *Energy Environ. Sci.* **2013**, *6*, 1772–1778.
- (33) Freunberger, S. A.; Chen, Y.; Drewett, N. E.; Hardwick, L. J.; Barde, F.; Bruce, P. G. The Lithium–Oxygen Battery with Ether-Based Electrolytes. *Angew. Chem., Int. Ed.* **2011**, *50*, 8609–8613.
- (34) Ramirez, I. R.; Cruz, A. M. Electrochemical Lithium Insertion in  $\beta$ -MoO<sub>3</sub>: Novel Li<sub>x</sub>MoO<sub>3</sub> Bronzes. *J. Solid State Electrochem.* **2003**, *7*, 259–263.
- (35) Bullard, J. W.; Smith, R. L. Structural Evolution of the MoO<sub>3</sub> (010) Surface During Lithium Intercalation. *Solid State Ionics* **2003**, *160*, 335–349.
- (36) Tsiouvaras, N.; Meini, S.; Buchberger, I.; Gasteiger, H. A. A Novel On-Line Mass Spectrometer Design for the Study of Multiple Charging Cycles of a Li–O<sub>2</sub> Battery. *J. Electrochem. Soc.* **2013**, *160*, A471–A477.